

Daniel R. Clymer

Mem. ASME

Department of Mechanical Engineering,
Carnegie Mellon University,
5000 Forbes Avenue,
Pittsburgh, PA 15213
e-mail: dcllymer@andrew.cmu.edu

Jonathan Cagan

Mem. ASME

Department of Mechanical Engineering,
Carnegie Mellon University,
5000 Forbes Avenue,
Pittsburgh, PA 15213
e-mail: cagan@cmu.edu

Jack Beuth

Department of Mechanical Engineering,
Carnegie Mellon University,
5000 Forbes Avenue,
Pittsburgh, PA 15213
e-mail: beuth@andrew.cmu.edu

Power–Velocity Process Design Charts for Powder Bed Additive Manufacturing

A current issue in metal-based additive manufacturing (AM) is achieving consistent, desired process outcomes in manufactured parts. When process outcomes such as strength, density, or precision need to meet certain specifications, changes in process variable selection can be made to meet these requirements. However, the changes required to achieve a better part performance may not be intuitive, particularly because process variable changes can simultaneously improve some outcomes while worsening others. There is great potential to design the additive manufacturing process, tailoring process variables based on user requirements for a given part. In this work, the tradeoffs between multiple process outcomes are formalized and the design problem is explored throughout the design space of process variables. Based on user input for each process outcome considered, P–V (power–velocity) process design charts are introduced, which map the process space and identify the best combination of process variables to achieve a user's desired outcome. [DOI: 10.1115/1.4037302]

Introduction

Direct-metal additive manufacturing (AM) is a rapidly expanding manufacturing method that has found applications within the fields of aerospace, medicine, and others requiring highly complex structures. Within metal-based AM, the powder bed processes have generated significant interest due to their ability to obtain high precision and tolerance. There are two main branches of powder bed AM and they are distinguished by their power source: selective laser sintering (SLS) and electron beam melting (EBM) systems. Another major difference between SLS and EBM is that SLS operates in an inert gas environment, while EBM operates in a vacuum. This study will focus on the SLS process through methods that are extendable to EBM and nonpowder bed AM processes.

Metal-based AM in general is a relatively new form of manufacturing, and a lack of good process knowledge in the field can cause build results to be more variable than traditional manufacturing methods, thereby limiting its capability. To utilize the full potential of AM as an alternative manufacturing method, it is necessary to have sound understanding about how a part will be affected by its process variable selection. Careful selection of process variables can be a deciding factor in whether a part meets its performance requirements or not and can greatly affect part quality.

Individual outcomes of the AM process have recently been studied, including microstructure [1], surface finish (SF) [2], and residual stresses [3]. Various process variables have been considered, including beam properties [4], scan strategy [5], layer thickness, build orientation [6,7], and particle size [2]. AM processes have been mapped to examine the effect of process variables on melt pool characteristics [1,8]. Much of this current research has given users a better understanding of the available design space in AM and shown how various process selections can improve properties of interest. In contrast, this study examines the situation when multiple outcomes integral to the product's manufacturing quality must be balanced in the same build.

Often in direct-metal AM, the two most significant process variables are the beam absorbed power (P) and beam travel velocity

(V). These variables have the most impact on the rate of heat entering the system and therefore are the most important for the transient heat conduction problem. In this research, the behavior of several process outcomes (density, yield strength, surface finish, precision, and deposition rate) is predicted within the P – V design space. A design tool is introduced, based on user requirements for each outcome, which finds regions of P – V space satisfying the user requirements and identifies the optimal choice within those regions. This tool provides the process designer with more confidence and control over the combination of outcomes achievable from the part being built. As is outlined in several case studies, these results can direct the user to a choice of beam power and velocity that is different than the machine nominal settings, resulting in a better part. The design tool introduced in this work attempts to find the ideal tradeoff in process variables in metal-based AM, resulting in P – V process design charts to identify the best overall part properties.

Methods

The desired result of this study is to find the best process variable combination based on a user's input for several process outcomes. The process outcomes included in the study are: density, yield strength, surface finish, precision, and deposition rate. These have been included because they are outcomes that are often considered important to part designers. The process variables are absorbed power (P) and beam scanning velocity (V). Through several basic assumptions about the AM process, each outcome is tied back to these two process variables, and equations are created, which show how each outcome is expected to change throughout P – V space. For illustration, in this paper outcomes are calculated for type 316L stainless steel fabricated by a SLS process, applicable to a raster geometry used to fill in the interior of solid layers, and using an assumed preheat temperature of 100 °C. However, similar methods could be applied for other materials and processes, other deposition geometries (e.g., contours on external surfaces of layers), and other preheat temperatures.

Assumptions. In order to tie each process outcome calculation back to the power and velocity inputs, a series of assumptions are made about the hatch spacing, layer thickness, and material absorptivity in the SLS process.

Contributed by the Design for Manufacturing Committee of ASME for publication in the JOURNAL OF MECHANICAL DESIGN. Manuscript received December 19, 2016; final manuscript received May 31, 2017; published online August 30, 2017. Assoc. Editor: Paul Witherell.

Hatch Spacing and Layer Thickness. The layer thickness (thickness of the new powder layer) and hatch spacing (the distance between the centers of the deposited beads) are variables that can be changed on the machine. However, both variables will typically scale with the melt pool size. This is because the layer thickness and hatch spacing need to be smaller than the melt pool depth and width, respectively, for all the materials to be fully melted. Once a factor of safety is chosen, good choices for the layer thickness and hatch spacing can be determined by the melt pool size. In this work, the ratio of layer thickness to melt pool depth is assumed to be 1/5, to provide a sufficient overlap between layers.

For a given melt pool shape and size, a certain fraction of hatch spacing to melt pool width (MPW) exists such that the maximum rate of material melting occurs. The work by Tang et al. [9] has found that for melt pools with a semicircular cross section normal to the velocity direction, this optimal fraction of hatch spacing to melt pool width is $(\sqrt{2}/2)$. This fraction is used to relate hatch spacing back to the melt pool size, which is determined from the laser power and velocity input settings from the user. In practice, variations in melt pool shape in different regions of P - V space will cause variations in the ideal hatch spacing fraction, as discussed by Gong et al. [10] in their 2014 melt pool characterization work. Work to characterize melt pool size and shape across process input parameters, such as that done by Beuth et al. [8] and Cheng and Chou [11], will help to improve this baseline model in future work.

Absorptivity. The absorptivity of the metal powder determines what percentage of the beam power is absorbed into the melt pool during the process. The calculations in this study use absorbed power, assuming that the absorptivity is already taken into account. Thus, the instances where absorptivity must be considered are where the absorbed power is related back to the machine settings, namely, the maximum power and the nominal power settings. For these calculations, a thermal absorptivity of 0.5 is assumed for stainless steel 316L powder, comparable to the value of about 0.58 found by Rubenchik et al. [12]. This study considered an SLS process with a maximum achievable power of 400 W and a nominal power setting of 195 W for stainless steel 316L, resulting in a maximum absorbed power of 200 W and nominal absorbed power of 97.5 W.

Melt Pool Calculations. To calculate the process outcomes, the melt pool sizes must be predicted throughout P - V space. Finite element simulations, modeling the laser powder process, were run using ABAQUS software and predicted melt pool quantities throughout P - V space. This model was similar to the model created by Soylemez and coworkers [13], or more recently, Montgomery et al. [14], but for stainless steel. The model simulated a distributed heat source scanning over a substrate of stainless steel 316L. The other surfaces in the model were maintained at a boundary condition temperature corresponding to the background temperature of the process, 373 K. This background temperature was assumed to be constant. A symmetric boundary condition was imposed on the midplane to reduce computation time. These simulations are applicable to raster scanning in the interior of solid layers. To account for more complex geometries or scan patterns in which melt pool dimensions would be expected to change, a greater range of simulations would need to be performed to characterize these circumstances, such as discussed by Beuth et al. in their AM process mapping work [8].

These simulations solved the transient heat equation for conduction throughout the substrate. Radiation and convection, for the SLS process being considered, are also modes of heat transfer within the build chamber. However, models by Roberts et al. [15] for the SLS process, as well as Shen and Chou [16] for the EBM process, suggest that these modes of heat transfer are insignificant compared to conduction in the system.

Using the simulations discussed, melt pool properties were calculated for six P - V combinations, which were 50 W–200 mm/s, 50 W–500 mm/s, 50 W–1400 mm/s, 200 W–200 mm/s, 200 W–

500 mm/s, and 200 W–1400 mm/s. These six points can be used to map out P - V space in terms of the melt pool characteristics. This type of mapping has been observed to closely follow the real behavior throughout P - V space of a direct-metal AM-produced material [13]. All the calculations in this research are done for stainless steel type 316L.

Process Outcome Calculation. The process outcomes considered in this study were density, yield strength, surface roughness, precision, and deposition rate. Curves for each of these outcomes were tied back to experimental results found for type 316L stainless steel.

Porosity and Susceptibility to Flaws. Achieving full density is typically one of the most important requirements for an additively manufactured part. If flaws caused by lack of fusion occur in the material during deposition, the part may not satisfy other material property requirements like monotonic strength or fatigue life. One way to limit the porosity is remelting each layer during the build [17], although this can greatly increase build time and cost.

The likelihood of porosity is related to how much overlap there is between the scanning melt pool and the top of the previous layer. Particularly, because there is some variability in the size of each melt pool, flaws will occur much more often if the melt pool depth is close to the same size as or smaller than the layer thickness. Note that because the powder layer will shrink by as much as 55% when it is melted [18], the effective layer thickness (the thickness of powder the melt pool has to melt through) will be larger than the actual resulting layer thickness.

Spierings et al. [19] found a correlation between the energy density supplied to the powder layer and the resulting density of the part with bulk geometry. The energy density, given in Eq. (1), takes laser power, velocity, hatch spacing, and layer thickness into account

$$\text{energy density} = \frac{P}{v \times h \times t} \quad (1)$$

The approximate relationship between energy density and part density from Ref. [19] is given in the below equation

$$\text{part density (\%)} = (0.92 + 12.2a - 514a^2 + 4318a^3) \times 100\% \quad (2)$$

where h is the hatch spacing, t is the layer thickness, and $a = 1/(\text{energy density})$. With lower energy density, more flaws are likely to develop in the part. This means that more flaws would be expected to develop in the build at lower laser power and at higher scanning velocity settings. This relationship has been observed in other work, such as that done by Li et al. [20] on the density in AM-fabricated stainless steel. Also, note the dependence on hatch spacing and layer thickness: changing these can help fix porosity problems even with low power settings. Currently, a typical lowest layer thickness available on an SLS machine is 20 μm .

In this research, the energy density criterion described earlier is used to calculate P and V 's effect on density. The layer thickness is constrained to stay above the minimum value of 20 μm , meaning that any porosity issues occurring at that point could not be fixed by modifying the layer thickness settings. It should be noted that this criterion is an approximation and it does not explicitly take into account the geometry of the overlap between individual melt pool beads. A geometric analysis of bead overlaps and their effect on layer melting are needed to more precisely control lack of fusion porosity [21]. The resulting contour plot of percent density throughout P - V space is shown in Fig. 1. The low power, high velocity region in the lower right is expected to yield the most lack of fusion flaws.

Note that another source of porosity, "keyhole" mode melting, has often been observed to occur in the high power, low-velocity range in P - V space [22]. Recent work by Francis [23]

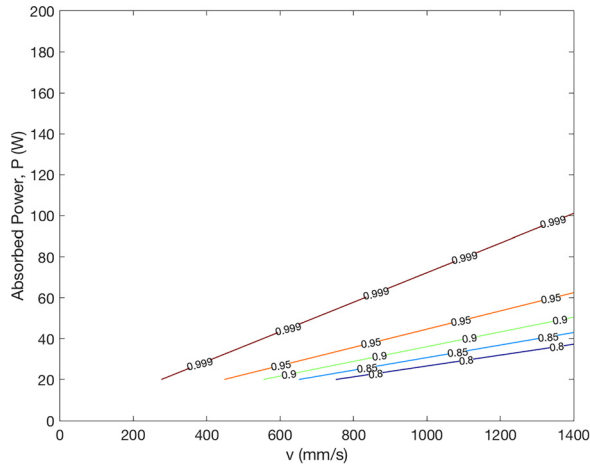


Fig. 1 Contour plot of expected density relative to full part density throughout P - V space

demonstrated the ability to avoid keyholing by changing the laser spot size to scale with the melt pool width. This work makes the assumption that the user is able to change the spot size to control keyholing in this region of P - V space, leaving lack of fusion as the remaining major source of porosity.

Yield Strength. Additively manufactured austenitic stainless steel has been observed to form a fine microstructure, due to the high cooling rates characteristic of the AM process [24–27]. Although a detailed model has not been created to describe yield strength dependence in processing space, it has been shown that this microstructure gets finer with faster characteristic cooling rates, and that the strength increases with these finer microstructures [26,28]. Wang et al. [28] performed SLS tests on austenitic stainless steel type 304L and used a Hall–Petch relationship to explain the resulting yield strengths for different processing input settings. The Hall–Petch model, which states that there exists an inverse square root relationship between yield strength and grain size in a material, was also used as the governing equation for yield strength in this research. This relationship occurs because moving dislocations, which cause material yielding, are impeded at the grain boundaries. This makes materials with smaller grains (more grain boundaries) stop dislocation movement better and therefore take more applied stress before yielding. The Hall–Petch equation is given below

$$\sigma = \sigma_0 + K_H d^{-1/2} \quad (3)$$

where σ is the yield strength, d is the grain size, and σ_0 and K_H are the constants. The values for σ_0 and K_H used are 150.8 MPa and $575.0 \text{ MPa } \mu\text{m}^{1/2}$, respectively, taken from experimental results found by Singh et al. [29]. Using this expected trend, a contour map of the expected trend in yield strength throughout P - V space is shown in Fig. 2.

Surface Finish. Surface finish is typically defined in terms of R_a , which is the average of the absolute value of the profile height deviations from the mean height of a surface [30]. Spierings et al. [2] showed that the as-built R_a of an AM part with simple geometry scales with the average particle size of the powder in metal-based AM. Assuming a linear scaling (we expect particles half the size to have half the R_a value), the expected trend can be predicted throughout P - V space. The equation used for surface finish is given below

$$\text{SF} = C \times D \quad (4)$$

where SF is the surface finish, D is the average particle diameter, and C is a constant depending on material. Furthermore, the

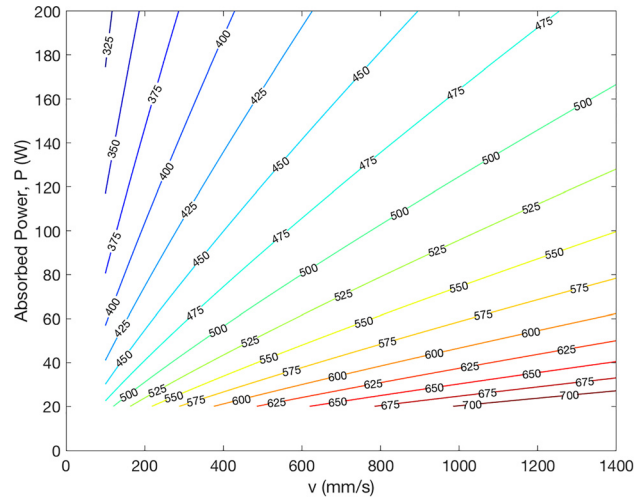


Fig. 2 Contour plot of yield strength (MPa) relationship throughout P - V space

powder size is assumed to be constrained by the size of the layer thickness, because the largest particles must fit under the recoater blade when a new layer of powder is spread during the SLS process. As discussed in the “Assumptions” section, the layer thickness is then related back to the melt pool depth of the process, which was ultimately tied back to the P - V inputs through simulation. This expected trend was fit to data from the EOS data sheet for 316L stainless steel [31], which provided typical experimental results for parts built at the nominal settings. From this source, as-built parts at the nominal settings on the machine achieved R_a values of $13 \pm 5 \mu\text{m}$. The expected trend, fit to this data point, is shown in Fig. 3.

Precision. The obtainable precision refers to the accuracy to which the machine can reliably deposit during the build (e.g., the accuracy to which the dimension of an edge can be deposited). This value scales with the average width of the melt pool, because the process is only capable of creating features that are bigger than one of the melt pools [32]. The equation used to govern precision changes throughout the domain is given below

$$P = C \times \text{MPW} \quad (5)$$

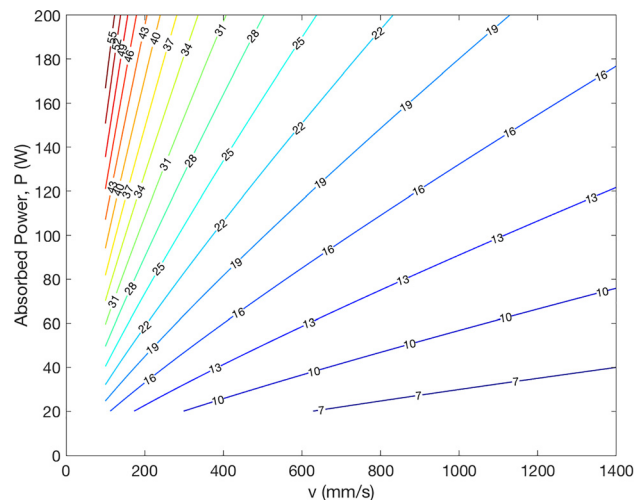


Fig. 3 Contour plot of surface finish (μm) relationship throughout P - V space

where P is the precision, MPW is the melt pool width, and C is a constant. According to the EOS data sheet for 316L stainless steel, a precision of about $35\text{ }\mu\text{m}$ is typically achieved at the nominal settings for basic geometries [31]. Using this data point as a guide, and simulation results yielding a melt pool width at nominal settings equal to $74\text{ }\mu\text{m}$ and a resulting value of $C = 0.47$, trends like those shown in Fig. 4 can be expected to reflect the change in precision throughout P - V space.

Deposition Rate. The deposition rate is the rate at which new melted material is being added to the part. Shi et al. [33] gave a benchmark equation to calculate the expected deposition rate, which is given below

$$\text{DR} = t \times h \times v \quad (6)$$

where t is the layer thickness, h is the hatch spacing (distance between the center of two beads), and v is the beam scanning velocity. As discussed in the "Assumptions" section, the layer thickness is assumed to scale by $1/5$ of the expected melt pool depth, and the optimal hatch spacing should be $(\sqrt{2}/2)$ of the melt pool width. Using the simulation predictions of melt pool size, deposition rate follows a trend in P - V space similar to Fig. 5.

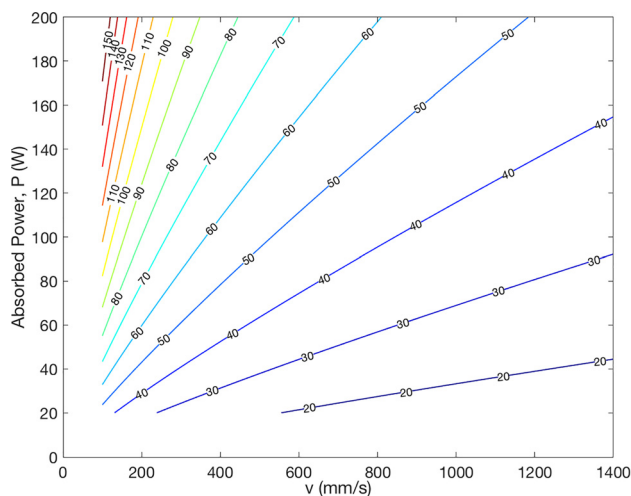


Fig. 4 Contour plot of precision (μm) relationship throughout P - V space

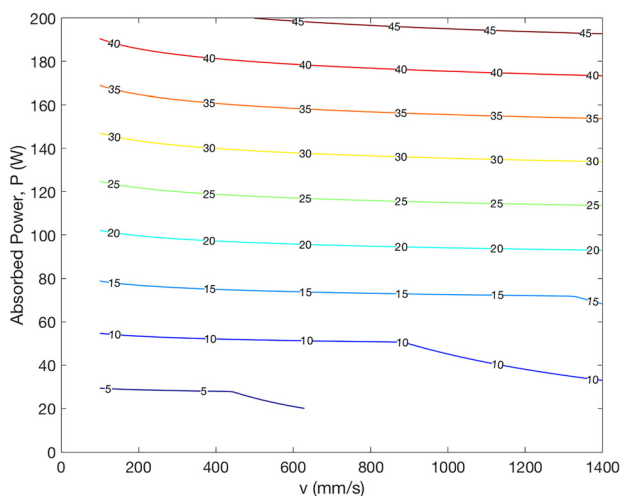


Fig. 5 Contour plot of deposition rate (mm^3/s) relationship throughout P - V space

Note that the deposition rate depends strongly on the absorbed power of the substrate and weakly on the velocity of the beam. This is distinctive from the other four considered process outcomes that essentially depend on the characteristic melt pool size of the process. The lower right corner of the process map becomes more velocity dependent because, for the SLS process discussed in this study, the layer thickness cannot be decreased past $20\text{ }\mu\text{m}$ to accommodate for the smaller melt pools in that region.

The Multi-Objective Problem. A major goal of this work is to create a function that takes user requirement for an AM part and guides them to the best process variables for their application. In this study, there are five process outcomes that are being considered. Since each of these process outcomes is being simultaneously considered by the user, this problem can be thought of as a multi-objective design problem, where each process outcome is a design objective.

A common multi-objective optimization approach is called the bounded-objective function method [34]. This method optimizes one of the objective functions, while using each of the remaining objectives to form an additional constraint. This method requires user knowledge of requirements for each objective and the feasibility of converting all but one objective function into constraints. In the context of this study, this method applies and incorporates a user requirement on the maximum or minimum acceptable value for each converted objective, resulting in a process constraint, and finds a window in processing space that satisfies all these requirements. Inside the new constrained space, the final objective function remains and is then optimized. In this study, a bounded-objective function approach to the additive manufacturing process will be introduced.

P - V Process Design Charts. Incorporating the models and assumptions for each of the considered process outcomes, a design tool called P - V process design charts was developed to guide AM users toward P - V choices that best aligned with their requirements. The basic concept of the design tool is to treat the AM process as a bounded-objective optimization problem, treating all but one of the considered process outcomes as a constraint, and optimizing the final outcome within the constrained space created by satisfying all other outcomes.

The algorithm takes user requirements for all but one process outcome and, using the models discussed in the "Methods" section, finds the curve for each process outcome that will satisfy its requirement. Each of these curves is treated as an inequality constraint, with the space on one side of the curve satisfying, and the space on the other side of the curve not satisfying its corresponding user requirement. Each inequality constraint is overlaid onto one P - V chart. Depending on the user inputs, if there exists a region that can satisfy all inequality constraints, it is identified (shaded in), representing a processing window in P - V space that can satisfy all user requirements. This processing window typically represents a smaller subset of P - V combinations out of all the combinations that a user could choose.

Within the resulting processing window, the final outcome that does not have a corresponding user requirement is optimized to direct the user to the best P - V combination within the window. A contour plot of this final objective is also overlaid on the chart to show how the objective changes throughout the P - V space. The final output is a P - V process design chart, with domain and range representing the range of input settings on the machine, overlaid with a shaded region, representing the subset of P - V combinations that satisfies the user's build requirements, finally overlaid with a contour plot of the remaining objective, illustrating to the user the ideal processing conditions for their needs, and comparing that to the machine nominal settings for the material and process.

An important part of the final result is the visual aspect of showing the P - V process design chart as opposed to a simpler output of suggested P and V values to the user. The chart is useful to

the user for several reasons: First, it illustrates which constraint is active (which constraint, if relaxed, would change the location of the optimum). A visualization of how far each constraint boundary is from the optimum shows the user which changes to requirement inputs would significantly change the solution and which are not significant to the solution for that case. In cases where no region can be found that satisfies all requirements, the graphical output can show the user which requirements would most likely need to be changed to allow for a solution. Second, the P - V process design chart output shows the user the relative size of the processing window in relation to the range of possible input parameters as well as in relation to the nominal settings. A smaller processing window can indicate a higher difficulty of achieving all requirements for a build and can prompt the AM user to change requirements before risking a failed build. Third, a plot of the objective contours around the optimum shows the user the robustness of the solution; shallower contours represent a solution that is more resilient to small changes in process input settings. This may influence the user's final decision on process variables toward a more robust, albeit suboptimal, selection, particularly for AM processes that have more variable build results compared to other manufacturing methods.

Results

Case Study #1. As a first example, consider a part that will have small features, requiring tight precision tolerance as well as a tight regulation on part density. For illustration, requirements are shown in Table 1.

After satisfying each of these requirements, it is desired to maximize the build rate. Figure 6 shows a P - V process design chart of build rate in P - V space overlaid with each constraint requirement. The shaded region shows the area that satisfies all build requirements. In this case, the yield strength constraint is active. The optimum within that region is in the upper right, where the build rate is maximized.

A designer for additive manufacturing could use this information to alter the process input variables to achieve a part more closely aligned with their required output. In this example, there is a relatively large region that satisfies all constraints, indicating

Table 1 Case study #1 requirements

Surface finish (Ra)	Less than 25 μm
Precision	Less than 50 μm
Density	At least 99.5%
Yield strength	Greater than 490 MPa
Maximize build rate	

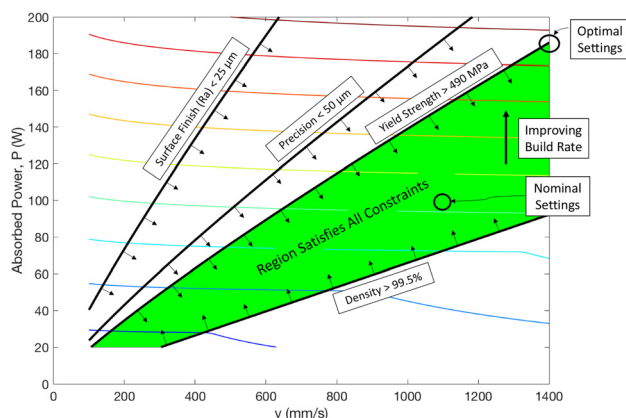


Fig. 6 Case study #1, a P - V process design chart showing objective contours of build rate overlaid on design constraint requirements

that many different P - V combinations could satisfy the user requirements. However, the optimal P - V combination that was found, which maximized the build rate while satisfying each constraint, is $P = 186 \text{ W}$, $V = 1400 \text{ mm/s}$. This deviates from the machine nominal settings for 316L stainless steel, which are $P = 97.5 \text{ W}$, $V = 1083 \text{ mm/s}$. The P - V process design chart provides feedback on which constraints, if relaxed somewhat, would change the optimal solution, and which would not affect the optimum. In this example, relaxing the constraint on yield strength would change the location of the optimum. Constraints such as surface finish or density could be significantly changed before they would affect the optimal solution.

Case Study #2. In case study #2, consider a part that has a high requirement on surface finish and also needs to be built quickly. Example requirements for this case are shown in Table 2.

After meeting these constraints, the objective is to maximize the obtainable precision in the process. The resulting P - V process design chart and identified optimum are shown in Fig. 7.

In this example, the active constraint is the build rate, with an optimal precision of 30.1 μm , located at $P = 92.9 \text{ W}$, $V = 1400 \text{ mm/s}$. Compared to the nominal machine settings where $P = 97.5 \text{ W}$ and $V = 1083 \text{ mm/s}$, the optimum is located in a region resulting in smaller melt pools. The contours of the objective, in this case precision, are shallow in the region of the optimum. This informs the user that the solution for this case study is robust; small variations in the input parameters would only slightly change the value of the optimum. This is a valuable information to the AM user, as it is an indicator of the reduced risk involved in making the processing decision.

Case Study #3. In a third example, consider the requirements in Table 3. It is desired to maximize the deposition rate upon meeting these constraints. The resulting P - V process design chart is shown in Fig. 8.

The results in Fig. 8 show that no region in P - V space can satisfy all of these requirements at once. This leaves the designer with a problem. For a solution to be possible, either the part will need to be redesigned to have different requirements (e.g., adding

Table 2 Case study #2 requirements

Surface finish (Ra)	Less than 18 μm
Deposition rate	At least 2 mm^3/s
Density	At least 99%
Yield strength	Greater than 450 MPa
Maximize precision	

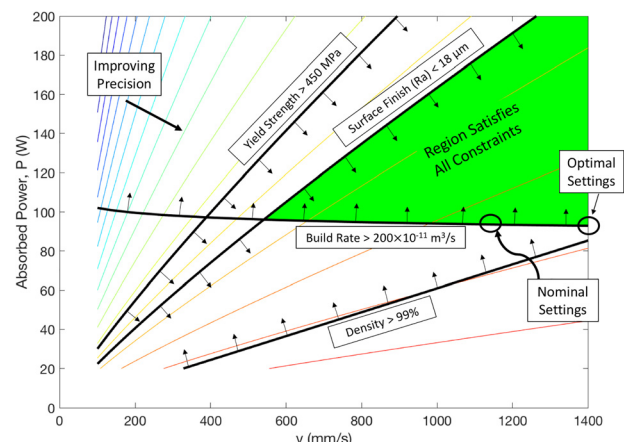
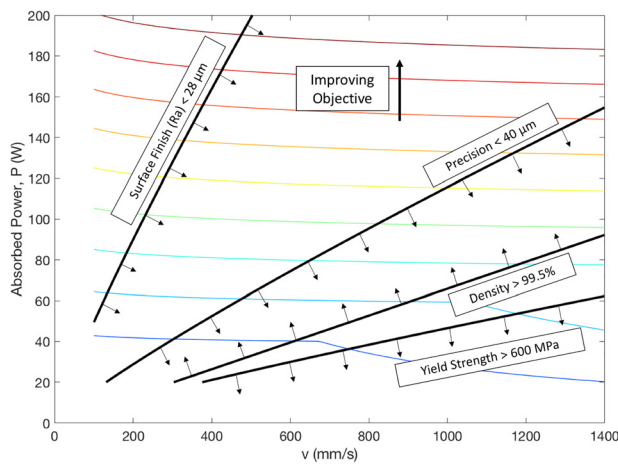


Fig. 7 Case study #2, a P - V process design chart showing objective contours of precision overlaid on design constraint requirements

Table 3 Case study #3 requirements

Surface finish (Ra)	Less than 28 μm
Precision	Less than 40 μm
Density	At least 99.5%
Yield strength	Greater than 600 MPa
Maximize build rate	

**Fig. 8 Case study #3, a P - V process design chart showing objective contours of build rate overlaid with design constraint requirements**

more material to decrease required yield strength) or some of the constraints will need to get relaxed. This kind of result gives the user valuable information about expected build outcomes before the time and money of performing actual builds have been spent.

Discussion

This study introduced the P - V process design chart as a design tool to assist an AM user in finding the best regions of P - V operating space: specifically, using a bounded-objective function method to guide the AM machine user toward a processing window that satisfies their specific requirements, ultimately providing more control over the outcome of the process. Typically, the results from this design tool will suggest a deviation from the nominal machine settings in order to achieve a build result more closely aligned with the desired outcomes. There is no global input setting that is optimal across all the cases; the optimal process inputs vary based on the user's unique requirements. The method proposed in this study gives the AM user greater understanding and control of the AM process in terms of the process outcomes important to them. As the AM field grows, this potential to control the design of the process in addition to the design of the geometry will make AM viable for more applications.

In the case studies presented in this paper, the results suggested a deviation away from the machine nominal settings, which for these examples is $P = 98$ W, $V = 1083$ mm/s. This demonstrates the fact that these process variables can be tailored for each specific situation, to create better design outcomes than would have resulted from the nominal settings, depending on user requirement for that situation. These examples also demonstrated the concept of a processing window that the user could operate within to satisfy their process requirements. This kind of design tool is especially useful for situations when users know exactly what requirements they need to meet to have a successful part.

Although the optimal process variables tend to deviate from the machine nominal settings, the machine nominal settings will often fall inside the processing window. This is because the nominal settings were likely selected to achieve acceptable results for a wide range of requirements. However, for specific situations,

these nominal settings will not necessarily be the best choice of process variables. A process that is designed with user requirements in mind, that varies from case to case, can achieve better outcomes for each case than a machine operating nominally. Furthermore, a P - V process design chart that illustrates both the requirements as well as the expected improvement can provide the AM user greater confidence and control over the build of the part meeting their expectations.

Because additive manufacturing is such a new technology, coupled with the fact that most users do not deviate from the nominal process variables, much work still needs to be done to characterize different AM processes and materials. Current models of processing space are often limited to simple part geometries and basic scan strategies. In the future, it will be of great use to the designer to have more comprehensive models that allow them to apply the proposed process design techniques to a wider range of part complexity. In this work, general expected trends are used as an example to show how a designer might formulate the problem of process design. Experimental results over the full range of process inputs are needed to fully validate these predictions, although the trends are expected to be similar. Future experiments will also contribute toward better understanding of process outcome variability and robustness, which can be incorporated into the P - V process design chart framework.

Another potential of the process design charts presented in this work is to be coupled with the 3D geometry of the part. Instead of solving for one set of parameters for the whole part, each region of the part would be solved separately. This would allow for parameters such as surface finish to be weighted very low in the interior of the part, while still being accounted for on the outer surface. Furthermore, this would enable the process designer to take advantage of and optimize AM's capability to create parts with variation in properties over the volume.

This work focused on the SLS process and stainless steel material as examples to illustrate a method of applying design principles to AM processes. However, using P - V process design charts to map out important outcomes can be applied to a wide range of AM processes and materials. As characteristics become available for other materials and processes, the models used for the examples in this work can be easily substituted with different models to guide AM users toward better process design for any number of AM processes. Ultimately, the framework presented in this paper is designed to increase the AM user's confidence and ability to tailor the AM process for their needs, and this goal will be significantly strengthened as more comprehensive governing models are developed in the future.

Conclusions

One of the most appealing aspects of additive manufacturing is the ability for builds to be customized specifically to a user's application. Currently, AM processes operating at the nominal settings are not reaching their full potential. In this paper, P - V (power-velocity) process design charts were introduced to enable previously developed process mapping techniques to define the P - V design space in additive manufacturing. Using P - V process design charts has produced insight into how an AM user might better approach the selection of process variables to enable optimal or robust process outcomes tailored to the user's needs. A real part will typically have multiple process outcomes that need to be simultaneously improved. The design tool presented in this work uses P - V process design charts to illustrate to the user how important process outcomes relate to each other, and what changes can be made to improve build results, particularly when compared to results at the nominal settings.

In the future, as more research is done to improve the field's understanding of process outcomes' relationship to process variables in AM, the assumptions made in this paper will be refined to give more precise results. Those assumptions and additional process variables and processes could be incorporated into the P - V

process design chart, resulting in more freedom to the process designer to build an optimal part, enabling greater user customization.

References

- [1] Gockel, J., and Beuth, J., 2013, "Understanding Ti-6Al-4V Microstructure Control in Additive Manufacturing Via Process Maps," *Solid Freeform Fabrication: An Additive Manufacturing Conference (SFF)*, Austin, TX, Aug. 12–14, pp. 666–674.
- [2] Spierings, A. B., Herres, N., Levy, G., and Buchs, C., 2011, "Influence of the Particle Size Distribution on Surface Quality and Mechanical Properties in Additive Manufactured Stainless Steel Parts," *Rapid Prototyping J.*, **17**(3), pp. 195–202.
- [3] Peter Mercelis, J. K., 2006, "Residual Stresses in Selective Laser Sintering and Selective Laser Melting," *Rapid Prototyping J.*, **12**(5), pp. 254–265.
- [4] Murr, L., Martinez, E., Medina, F., Gaytan, S. M., Ramirez, D. A., Hernandez, J., Amato, K. N., Shindo, P. W., and Wicker, R. B., 2012, "Metal Fabrication by Additive Manufacturing Using Laser and Electron Beam Melting Technologies," *J. Mater. Sci. Technol.*, **28**(1), pp. 1–14.
- [5] Mertens, R., Clijsters, S., Kempen, K., and Kruth, J.-P., 2014, "Optimization of Scan Strategies in Selective Laser Melting of Aluminum Parts With Downfacing Areas," *ASME J. Manuf. Sci. Eng.*, **136**(6), p. 061012.
- [6] Snyder, J. C., Stimpson, C. K., Thole, K. A., and Mongillo, D. J., 2015, "Build Direction Effects on Microchannel Tolerance and Surface Roughness," *ASME J. Mech. Des.*, **137**(11), p. 111411.
- [7] Ulu, E., Korkmaz, E., Yay, K., Burak Ozdoganlar, O., and Burak Kara, L., 2015, "Enhancing the Structural Performance of Additively Manufactured Objects Through Build Orientation Optimization," *ASME J. Mech. Des.*, **137**(11), p. 111410.
- [8] Beuth, J., Fox, J., Gockel, J., Montgomery, C., Yang, R., Qiao, H., Reeseewatt, P., Anvari, A., Narra, S., and Klingbeil, N., 2013, "Process Mapping for Qualification Across Multiple Direct Metal Additive Manufacturing Processes," *Solid Freeform Fabrication: An Additive Manufacturing Conference (SFF)*, Austin, TX, Aug. 12–14, pp. 655–665.
- [9] Tang, M., Pistorius, P. C., and Beuth, J. L., 2017, "Prediction of Lack-of-Fusion Porosity for Powder Bed Fusion," *Addit. Manuf.*, **14**, pp. 39–48.
- [10] Gong, H., Gu, H., Dilip, J. J. S., Pal, D., Stucker, B., Beuth, J., Christiansen, D., and Lewandowski, J. J., 2014, "Melt Pool Characterization for Selective Laser Melting of Ti-6Al-4V Pre-Alloyed Powder," *Solid Freeform Fabrication: An Additive Manufacturing Conference (SFF)*, Austin, TX, Aug. 4–6, pp. 256–267.
- [11] Cheng, B., and Chou, K., 2013, "Melt Pool Geometry Simulations for Powder-Based Electron Beam Additive Manufacturing," *Solid Freeform Fabrication: An Additive Manufacturing Conference (SFF)*, Austin, TX, Aug. 12–14, pp. 644–654.
- [12] Rubenchik, A., Wu, S., Mitchell, S., Golosker, I., LeBlanc, M., and Peterson, N., 2015, "Direct Measurements of Temperature-Dependent Laser Absorptivity of Metal Powders," *Appl. Opt.*, **54**(24), pp. 7230–7233.
- [13] Soylemez, E., Beuth, J., and Taminger, K., 2010, "Controlling Melt Pool Dimensions Over a Wide Range of Material Deposition Rates in Electron Beam Additive Manufacturing," *Solid Freeform Fabrication: An Additive Manufacturing Conference (SFF)*, Austin, TX, Aug. 9–11, pp. 571–582.
- [14] Montgomery, C., Beuth, J., Sheridan, L., and Klingbeil, N., 2015, "Process Mapping of Inconel 625 in Laser Powder Bed Additive Manufacturing," *Solid Freeform Fabrication Symposium: An Additive Manufacturing Conference (SFF)*, Austin, TX, Aug. 10–12, pp. 1195–1204.
- [15] Roberts, I. A., Wang, C. J., Esterlein, R., Stanford, M., and Mynors, D. J., 2009, "A Three-Dimensional Finite Element Analysis of the Temperature Field During Laser Melting of Metal Powders in Additive Layer Manufacturing," *Int. J. Mach. Tools Manuf.*, **49**(12–13), pp. 916–923.
- [16] Shen, N., and Chou, K., 2012, "Thermal Modeling of Electron Beam Additive Manufacturing Process: Powder Sintering Effects," *ASME Paper No. MSEC2012-7253*.
- [17] Yasa, E., and Kruth, J., 2012, "Microstructural Investigation of Selective Laser Melting 316L Stainless Steel Parts Exposed to Laser Re-Melting," *First CIRP Conference on Surface Integrity (CSI)*, Bremen, Germany, Jan. 30–Feb. 1, pp. 389–395.
- [18] Steen, W. M., and Mazumder, J., 2010, *Laser Materials Processing*, Springer, London.
- [19] Spierings, A. B., Wegener, K., and Levy, G., 2012, "Designing Material Properties Locally With Additive Manufacturing Technology SLM," *Solid Freeform Fabrication Symposium: An Additive Manufacturing Conference (SFF)*, Austin, TX, Aug. 6–8, pp. 447–455.
- [20] Li, R., Shi, Y., Wang, Z., Wang, L., Liu, J., and Jiang, W., 2010, "Densification Behavior of Gas and Water Atomized 316L Stainless Steel Powder During Selective Laser Melting," *Appl. Surf. Sci.*, **256**(13), pp. 4350–4356.
- [21] Cunningham, R., Narra, S. P., Montgomery, C., Beuth, J., and Rollett, A. D., "Synchrotron-Based X-Ray Microtomography Characterization of the Effect of Processing Variables on Porosity Formation in Laser Power-Bed Additive Manufacturing of Ti-6Al-4V," *JOM*, **69**(3), pp. 479–484.
- [22] Rai, R., Elmer, J. W., Palmer, T. A., and DebRoy, T., 2007, "Heat Transfer and Fluid Flow During Keyhole Mode Laser Welding of Tantalum, Ti-6Al-4V, 304L Stainless Steel and Vanadium," *J. Phys. D: Appl. Phys.*, **40**(18), pp. 5753–5766.
- [23] Francis, Z., 2017, "The Effects of Laser and Electron Beam Spot Size in Additive Manufacturing Processes," *Ph.D. dissertation*, Carnegie Mellon University, Pittsburgh, PA.
- [24] Guo, W., and Kar, A., 1999, "Prediction of Microstructures in Laser Welding of Stainless Steel AISI 304," *J. Laser Appl.*, **11**(4), pp. 185–189.
- [25] de Lima, M. S. F., and Sankare, S., 2014, "Microstructure and Mechanical Behavior of Laser Additive Manufactured AISI 316 Stainless Steel Stringers," *Mater. Des.*, **55**, pp. 526–532.
- [26] Smugersky, J. E., Keicher, D. M., Romero, J. A., Griffith, M. L., and Harwell, L. D., 1997, "Laser Engineered Net Shaping (LENS™) Process: Optimization of Surface Finish and Microstructural Properties," Sandia National Laboratories, Albuquerque, NM, Report No. [SAND-97-8652C](#).
- [27] Yu, J., Rombouts, M., and Maes, G., 2013, "Cracking Behavior and Mechanical Properties of Austenitic Stainless Steel Parts Produced by Laser Metal Deposition," *Mater. Des.*, **45**, pp. 228–235.
- [28] Wang, Z., Palmer, T. A., and Beese, A. M., 2016, "Effect of Processing Parameters on Microstructure and Tensile Properties of Austenitic Stainless Steel 304L Made by Directed Energy Deposition Additive Manufacturing," *Acta Mater.*, **110**, pp. 226–235.
- [29] Singh, K. K., Sangal, S., and Murty, G. S., 2002, "Hall-Petch Behaviour of 316L Austenitic Stainless Steel at Room Temperature," *Mater. Sci. Technol.*, **18**(2), pp. 165–172.
- [30] Whitehouse, D., 2012, *Surfaces and Their Measurement*, Butterworth-Heinemann, Boston, MA.
- [31] EOS, 2014, "Material Data Sheet: EOS StainlessSteel 316L," *Electro Optical Systems GmBH*, Phoenixville, PA.
- [32] Adam, G. A. O., and Zimmer, D., 2014, "Design for Additive Manufacturing—Element Transitions and Aggregated Structures," *CIRP J. Manuf. Sci. Technol.*, **7**(1), pp. 20–28.
- [33] Shi, X., Ma, S., Liu, C., Chen, C., Wu, Q., Chen, X., and Lu, J., 2016, "Performance of High Layer Thickness in Selective Laser Melting of Ti6Al4V," *Materials*, **9**(12), p. 975.
- [34] Marler, R. T., and Arora, J. S., 2004, "Survey of Multi-Objective Optimization Methods for Engineering," *Struct. Multidiscip. Optim.*, **26**(6), pp. 369–395.